FISEVIER

Contents lists available at ScienceDirect

Materials & Design

journal homepage: www.elsevier.com/locate/matdes





Tailorable thermoelasticity of cubic lattice-based cellular and granular materials by prestress

Chao Liu, Huiming Yin*

Department of Civil Engineering and Engineering Mechanics, Columbia University, 610 Seeley W. Mudd, 500 West 120th Street, New York, 10027, NY, USA

ARTICLE INFO

Keywords:
Cubic lattices
Harmonic potential
Hertz's contact
Configurational stress
Effective elasticity
Effective thermal expansion coefficient

ABSTRACT

When a cubic lattice packaged by a boundary layer is subjected to a mechanical and temperature load, the force and length change of the bonds are equivalently evaluated by the average stress and strain of the unit cell. Provided a displacement gradient variation at a certain stress state, the variation of stress related to the strain variation provides the effective stiffness of the material at the corresponding configuration. It is discovered that the effective elasticity and thermal expansion coefficient can be tailored by the prestress through the boundary layer, which generates a configurational stress. Because the bonds of a cubic lattice depend on the material types, we consider the harmonic potential of springs for cellular lattices and Hertz's contact potential of balls for granular lattices, respectively. The cubic symmetry of effective elasticity is demonstrated for the three types of cubic lattices. By taking the orientational average, isotropic elastic constants can be obtained for randomly oriented lattices. As the bond length changes with the prestress of the boundary layer and controls the thermoelastic behavior, a novel design method of lattice-based materials confined in a spherical shell is demonstrated to achieve zero thermal expansion and a positive temperature derivative of elasticity.

1. Introduction

Cubic structures, such as face-centered cubic (FCC), body-centered cubic (BCC), and simple cubic (SC), are popular lattice structures, which are found in crystals, granular materials, or cellular lattices [1–3]. The emerging three-dimensional (3D) printing technology can fabricate materials with lattice structures in the laboratory as well [4–7]. The recent discovery showed that applying a prestress to lattice-based ultralightweight composites (ULWC) can change the thermoelastic behavior through the configurational stress [8,9], which creates a new way to fabricate a composite with zero thermal expansion coefficient and zero temperature derivative of stiffness, which may not exist in the natural materials.

For example, Fig. 1 shows an application of lattice materials to the Artemis project [10,11], which requires the transportation of building materials from the earth and the erection of the foldable tall structure on the south pole of the moon. The large temperature variation from -175 to 125 °C or even more exists in the structure during the service lifetime due to the nonuniform irradiation exposure in a vacuum environment [12–14]. It is crucial to use a lightweight, stiff, and temperature-insensitive material with a high buckling resistance to achieve the stability and economics of the structure [15,16]. In

Fig. 1(a), the ULWC balls are filled an aluminum tube, and a prestress is applied by the cap of the tube which causes compression in the granular lattice and tension in the tube in Fig. 1(b). One can tailor the thermoelastic constants and buckling resistance of the bar for the ultra-lightweight structural member and fabricate the foldable frame of the 50 kW PV array. Fig. 1(c) and (d) show the overview of the innovative technology of foldable structure and the entire system, respectively. This paper will show the mechanism of how to achieve zero thermal expansion coefficient and zero temperature derivative of stiffness of the composites.

The force transfer in the structure of a lattice material is through the bonds between the nodes of the network. At the macroscale, the lattice can be treated as a homogeneous material with a certain effective stiffness, which should be correlated with the forces and displacements of the bonds given the characteristics of the lattice structure.

A lattice-based material contains one-dimensional (1D) bonds connected into a 2D or 3D solid at the macroscale, and the stress transfer through the lattice is different from the continuum solids [17] that is typically modelled by the classical micromechanical models based on the stress homogenization of reinforcements in a continuous matrix [18–20]. For example, micromechanics-based models [21,22] treated the 1D components such as fibers as dispersed slender ellipsoids inter-

E-mail address: yin@civil.columbia.edu (H. Yin).

^{*} Corresponding author.

Fig. 1. Design of a lattice material based solar array structure for the Artemis Project: (a) The ULWC balls filled in a metal tube; (b) Prestress induced by the screw cap of the tube; (c) The ULWC filled tube used for a foldable frame, and; (d) The entire photovoltaic system.

acting with the matrix directly; while the lattice-based materials exhibit a continuous network of bonds for the force transfer, and no matrix phase is required. Although many papers in the literature addressed specific lattices with numerical simulations of the large truss frameworks [23–26], the models highly depended on the material design and computational resources.

Analytically modeling granular lattices dates back to the middle of the last century when Duffy and Mindlin studied the stress-strain relation for identical spheres packed in the face-centered cubic array [27], in which the contact force and displacements of a cubic unit cell are correlated through equilibrium and compatibility relations. This work was generalized to other regular packing patterns, such as simple cubic, tetrahedral, etc. [28–30]. With the use of the energy conservation approach, the secant stiffness tensor has been obtained for all regular packing patterns [31] as well. However, granular and cellular lattices have often been studied separately due to the different force-displacement relationships, for example, by finite element method (FEM) [25] and discrete element method (DEM) [32,33], respectively.

Considering the periodic structure of lattice-based materials, if the force-displacement relationship is well defined, the effective stiffness shall be unique and an exact solution may exist and be generic to different lattice-based materials. Actually, the lattice element method (LEM) [34] has been proposed to simulate a continuum solid by a connected truss frame of lattice elements, which can be considered as a DEM approach [35] to simplification of the mechanical behavior of solids. On the contrary, as lattice-based materials already have information available about the lattice structure and bond, the effective elasticity can surely be simulated by LEM, FEM, or DEM, among others [25,32,36], which often require an array of many unit cells and render numerical results with a certain accuracy. Using the unit cell of actual lattice, LEM can derive the effective elasticity based on the strain energy equivalency, but it limits to the linear elasticity [37] and the effect of prestress is not considered. An explicit, exact solution of the effective elasticity is still of significant interest in the material design and analysis of such lattice-based materials.

The singum model [38] uses the Wigner Seitz (WS) cell of the cubic structure as a continuum particle to represent the material and applies the potential-based bond forces for the lattice structure. Although the lattice-based solids can be evaluated by stress and strain at the overall material level, the force is essentially transferred through the bonds between the nodes. The singum model correlates singular forces in the discrete structure with the stress over the continuous volume. Therefore, the cubic structure with singular bond forces can be simulated by the fully contacted continuum particle system with stresses, and the singum model does provide the exact solution for the lattices with potential-based bond forces. For an example of metamaterials made of a physical truss system [39], the bonds are represented by springs with a harmonic potential. The singum model indeed provided an analytical

form of elasticity for the metamaterials and predicted the effect of the prestress on the elasticity [39]. The forces between the nodes of the cubic structure depend on the material types. Hertz's potential [40] and harmonic potential [39] have been demonstrated for 2D cellular and granular materials.

This paper generalizes the singum model to FCC, BCC, and SC lattices, and derives the effective stiffness based on the potential of the bonds. Cellular and granular materials are demonstrated with the linear elastic and Hertz's contact bonds, respectively. The effective elastic properties are verified with the numerical simulation. Using the spring length changing with pressure and temperature, we can predict the elasticity changing with pressure and temperature given the thermal expansion coefficient of the bond materials. The singum model can correlate the potential with the elastic moduli in a very straightforward fashion. When the lattice orientation randomly changes due to defects, by taking the orientational average, isotropic elastic constants can be obtained.

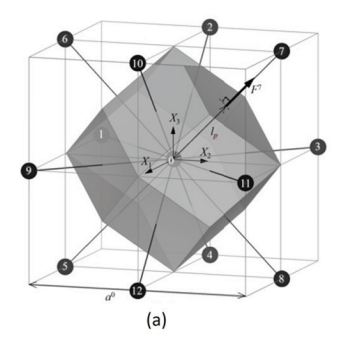
Particularly, a singum-based invention for material design [8] is introduced to package a lattice material with a boundary layer that provides a prestress to the lattice during the fabrication. Interestingly, the effective stiffness can be tailored by the prestress. When the temperature changes, the thermal expansion of the bond material will change the bond length as well as the confining stress in the boundary layer, which provides a novel design approach to zero thermal expansion and positive temperature derivative of elasticity of materials.

In the remainder of the paper, Section 2 introduces the construction of a singum particle using an FCC lattice as an example, and derives the elastic constants in terms of the derivatives of bond potential functions, which are generalized to BCC and SC as well. Section 3 demonstrates the model through a lattice material with linear spring bonds and granular material with Hertz's contact bonds. The explicit form of the effective elasticity of the lattices is provided. The effect of the configurational stress caused by the prestressing is discussed. Section 4 conducts a numerical simulation of the cubic lattices and verifies the exactness of the singum model. Section 5 demonstrates the applications of the singum model to lattice-based material design considering the effect of thermal expansion of materials with prestress. Some interesting results for the lattice-based material design for zero thermal expansion coefficient and positive temperature derivative of elasticity are demonstrated. A novel ultra-lightweight material with tailorable thermoelasticity is invented through a hierarchical lattice-based manufacturing process using cellular balls for a granular lattice.

2. Construction of the singum model for cubic lattices

2.1. The singum model for FCC cubic structure

Following the recent paper [41], we consider an FCC lattice in Fig. 2(a). Depending on the lattice material types, the bonds between



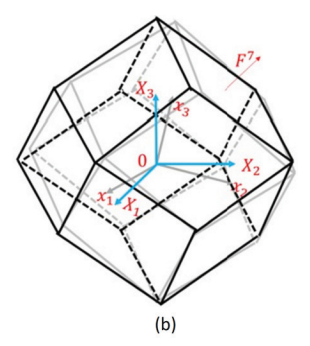


Fig. 2. The singum model of a face-centered cubic lattice: (a) the unit cell for the singum construction at the front central node with four more members not shown and; (b) the FCC singum of the WS Cell of the 0^{th} member in the initial configuration **X** (black lines) and the deformed configuration **x** (gray lines) [41].

the nodes can be Hertz's contacts, linear springs, or interatomic bonds. In the undeformed configuration, the unit cell of an FCC lattice exhibits the cubic edge length a^0 , so that the bond length between two neighbor nodes is $2l_p^0 = \frac{a^0}{\sqrt{2}}$ when the bond force is zero. We set up the Cartesian coordinate system with the origin at the 0th node, and 12 closest neighbor nodes are located at $(\pm \frac{a^0}{2}, \pm \frac{a^0}{2}, 0), (\pm \frac{a^0}{2}, 0, \pm \frac{a^0}{2}), (0, \pm \frac{a^0}{2}, \pm \frac{a^0}{2}),$ which are corresponding to the directional vectors \mathbf{n}^I $(I = 1, 2, ..., 12) = (\pm \frac{1}{\sqrt{2}}, \pm \frac{1}{\sqrt{2}}, 0), (\pm \frac{1}{\sqrt{2}}, 0, \pm \frac{1}{\sqrt{2}}),$ or $(0, \pm \frac{1}{\sqrt{2}}, \pm \frac{1}{\sqrt{2}})$. The singum particle is constructed by the Wigner Seitz (WS) cell [42] of the 0th node in Fig. 2(b) as a rhombic dodecahedron, in which each bond between the 0th node at the center and the 12 closest neighbor nodes is cut at the midpoint by a perpendicular plane. As shown in Fig. 2(b), a Cartesian coordinate \boldsymbol{X} is set up at the initial condition, i.e. the Lagrangian coordinates. After a homogeneous deformation of the lattice, the material points in X are referred to x at the deformed state, or the Eulerian coordinates, in which the lattice still keeps periodic, so that the whole space is still be filled with the deformed singums. Here because the outer surfaces of the singum particle are defined by the vertical planes of each bond, the singum particle maintains a polyhedral shape. Due to the central symmetry of the lattice, the nodes always keep in equilibrium under a uniform deformation. Without any loss of generality, the origins of x and X are both selected at the center of Node 0.

The above construction of the singum particle is simple and straightforward. The same procedure can be applied to all internal nodes of the lattice. However, the surface nodes cannot form singums because no bond exists beyond the surface. Instead, a boundary layer will be physically bonded to the surface nodes, which will be discussed in Section 5. Therefore, the singum particles are only constructed inside the material surface layer.

To formulate the singum model, we provide the following assumptions:

- 1. The interaction between nodes is governed by the bond potential $V(\lambda)$ where λ is the stretch ratio of the bond referred to as the undeformed bond length. At the zero-force bond length, $\lambda=1$; the hydrostatic deformation can be described by the bond length $\lambda=l_p/l_p^0$.
- 2. The interaction between two neighboring singums is through the surface stress vector along their interface edge, whose resultant force is equivalent to their bond force, i.e. $F_j = \frac{V_{,j}}{2l_p^0} n_j$. Here **F** and **n** denote the bond force and directional norm vector, respectively, along the same direction.
- The bonds form between the closest nodes only so that each node in FCC, BCC, and SC connects by 12, 8, and 6 bonds with the closest nodes accordingly. Therefore, each bond exhibits the same bond length.

Note that the resultant force on a singum from all neighboring singums is always zero due to the central symmetry of the bond forces so that the singum can maintain equilibrium automatically.

Consider Node 0 in the current lattice structure is in equilibrium. It is replaced by a singum particle in Fig. 2(b). Notice that although nodes 1–12 are located outside the singum, they are necessary parts to define the singum located at node 0, which are called "members" of the singum.

Consider the solid is made of the singums periodically and seamlessly filled in the space. The equilibrium equation in the absence of the body force or inertia force is written as:

$$\sigma_{ii,i} = 0 \tag{1}$$

where σ_{ij} is the stress tensor in a solid, which is applicable to the singum particle. The stress integral of the singum can be written as [19]

$$S_{ij} = \int_{v_e} \sigma_{ij}(\mathbf{x}) d\mathbf{x} = \sum_{I=1}^{12} x_i^I F_j^I$$
 (2)

where x_i^I indicates the coordinate of the cutting point of the bond, and $n_i^I = \frac{x_i^I}{|\mathbf{x}^I|}$ is the normalized direction vector component corresponding to \mathbf{x}^I . The distance between two neighboring nodes is defined as $r = 2l_p = 2|\mathbf{x}^I|$. The bond force can be written in terms of the derivative of the potential energy V as follows:

$$F_i^I = \frac{\partial V^I}{\partial r} n_i^I = \frac{\partial V^I}{\partial \lambda} \frac{\partial \lambda}{\partial r} n_i^I = \frac{V_i^I n_i^I}{2l_p^0}$$
 (3)

The displacement distribution can be described by the displacement gradient (DG) tensor, namely $d_{ij}=u_{j,i}$. Similarly, the integral of DG over the singum can be written as:

$$E_{ij} = \int_{v_s} d_{ij} d\mathbf{x} = \int_{v_s} u_{j,i} d\mathbf{x} = \int_{\partial v_s} n_i u_j d\mathbf{x} = \sum_{I=1}^{12} a_s^I n_i^I u_j^I$$
 (4)

where a_s^I is the plane surface area of the singum associated with the I^{th} bond, so $\sum_{I=1} 12 a_s^I = \partial v_s$. Here because all points on the same plane surface share the same \mathbf{n}^I and the displacement in a flat plane is linear, the displacement integral can be represented by the central point.

Therefore, the singum of Node 0 is constructed with the stress and DG integrals defined by the force and displacement of the cutting points on the singum surface. Note that the volume integrals of stress and DG in a continuum domain are transferred to its boundary [19]. Due to the flat plane of singum surface planes and Dirac Delta function as the point forces at the cutting points, the stress and DG are exactly obtained for the lattices with hinge connections, which creates a way to derive the stiffness of the lattices exactly.

To find the stiffness tensor C_{ijkl} , which correlates the stress and strain tensors, a DG variation, namely δd_{ij} , is applied to the singum, which produces the displacement variation on the singum through the Cauchy-Born rule [43] as

$$\delta u_i(\mathbf{x}) = \delta d_{ki} x_k = \delta x_i \tag{5}$$

The Eulerian strain variation caused by $\delta \mathbf{u}$ can be written as [41]:

$$\delta \varepsilon_{ij} = \frac{\delta d_{ij} + \delta d_{ji}}{2\lambda^2} \tag{6}$$

in which the higher order term of δd is disregarded because the paper aims to provide a simplified and analytical solution for the tangential stiffness. Compared to the above terms, the higher order term shall be disregarded as it is very small under small δu . Note that the assumption might not be suitable for relatively large strain conditions or nonlinear elastic analysis [44].

Note that the singum size of the cubic lattices changes with λ but maintains the same shape. However, the DG variation is an arbitrary

infinitesimal tensor to test the tangential elastic constants. The variation of volume can be described by DG variation as

$$\frac{\delta v_s}{v_s} = \delta d_{kk} \tag{7}$$

Given a variation of the cutting point δx_i^I , the force variation on the bond can be written as $\delta F_i^I = F_{i,j}^I \delta x_j^I$, where $F_{i,j}^I$ is the derivation of the force, from Eq. (3) as:

$$F_{i,j}^{I} = \frac{V_{,\lambda\lambda}^{I} \frac{\partial |\mathbf{x}^{I}|}{l_{p}^{0} \partial x_{j}} n_{i}^{I} + V_{,\lambda}^{I} \frac{\partial n_{i}^{I}}{\partial x_{j}}}{2l_{p}^{0}} = \frac{\lambda V_{,\lambda\lambda}^{I} n_{i}^{I} n_{j}^{I} + V_{,\lambda}^{I} (\delta_{ij} - n_{i}^{I} n_{j}^{I})}{2l_{p}^{0^{2}} \lambda}$$
(8)

where the following equation is used

$$n_{i,j}^{I} = \frac{\partial \frac{x_i^{I}}{lp}}{\partial x_j^{I}} = \frac{\delta_{ij} - n_i^{I} n_j^{I}}{l_p^0 \lambda} \tag{9}$$

Note that the origin of the coordinates is taken at the singum node. Although the stress distribution cannot be well defined on the singum, it can be measured on the singum through the average of the above stress integral as:

$$\sigma_{ij} = \frac{S_{ij}}{v_s} = \frac{\sum_{I=1}^{12} x_i^I F_j^I}{v_s}$$
 (10)

where $v_s = \lambda^3 v_s^0$ is the current volume of the singum. Because $x_i^I = l_p n_i^I$, one can write

$$x_i^I = \lambda l_n^0 n_i^I \tag{11}$$

The average stress can be obtained by taking the variation of Eq. (10) as

$$\delta\sigma_{ij} = \frac{1}{v_s} \sum_{I=1}^{12} \left(x_i^I F_{j,k}^I \delta x_k + F_j^I \delta x_i^I - x_i^I F_j^I \frac{\delta v_s}{v_s} \right)$$
 (12)

Note that the Cauchy stress variation includes three parts: the first part related to $F_{j,k}^I$ is caused by the force variation; whereas the second part δx_i^I and third part $\frac{\delta v_s}{v_s}$ related to F_j^I are the configurational stress caused by the existing force with the material configuration change. For the classic elasticity based on the infinitesimal deformation assumption, the effect of the configuration change on the material behavior has often been disregarded, but its effect is real and physical for lattice-based materials [40]. Substitution of Eqs. (3), (7), (8), and (11) into (12) yields:

$$\delta\sigma_{ij} = \frac{\sum_{I=1}^{12} \left[(\lambda^2 V_{,\lambda\lambda}^I - \lambda V_{,\lambda}^I) n_i^I n_j^I n_k^I n_i^I + \lambda V_{,\lambda}^I (\delta_{ik} n_l^I n_j^I + \delta_{jk} n_l^I n_i^I - \delta_{kl} n_i^I n_j^I) \right] \delta d_{kl}}{2v_s}$$

$$(13)$$

Because each bond exhibits the same length, the summation in Eq. (13) is reduced to the summation of $n_i^I n_j^I$ and $n_i^I n_j^I n_k^I n_l^I$, which can be written in the following identities for the FCC in Fig. 2 [41],

$$\sum_{l=1}^{12} n_i^I n_i^I = 4\delta_{ii}, \sum_{l=1}^{12} n_i^I n_i^I n_k^I n_l^I = (1 - \delta_{IK})\delta_{ii}\delta_{kl} + 2I_{iikl}$$
(14)

where $I_{ijkl} = \frac{1}{2}(\delta_{ik}\delta_{jl} + \delta_{jk}\delta_{il})$, and the terms with subscript indices including both uppercase and lowercase letters follow Mura's extended index notation as follows [18,20]:

- 1. Repeated lowercase indices are summed up as usual index notation;
- Uppercase indices take on the same numbers as the corresponding lowercase ones but are not summed.

Therefore, with the aid of Eqs. (6) and (14), Eq. (13) can be rewritten as:

$$\delta\sigma_{ij} = \frac{\lambda^2 \left[(\lambda^2 V_{,\lambda\lambda} - 5\lambda V_{,\lambda}) \delta_{ij} \delta_{kl} - (\lambda^2 V_{,\lambda\lambda} - \lambda V_{,\lambda}) \delta_{IK} \delta_{ij} \delta_{kl} + 2(\lambda^2 V_{,\lambda\lambda} + 3\lambda V_{,\lambda}) I_{ijkl} \right] \delta\varepsilon_{kl}}{2 v_s}$$

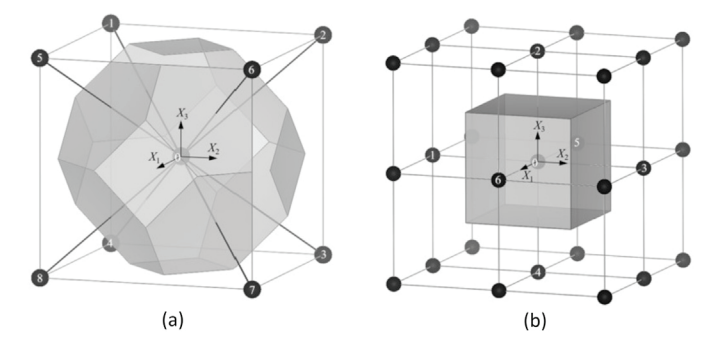


Fig. 3. The unit cells for the singum model construction at Atom 0: a bodycentered cubic lattice with 8 members (a) and a simple cubic lattice with 6 members (b).

Table 1 The singum variables for FCC, BCC & SC lattice with unit cell edge length a_0 .

Entities	FCC	BCC	SC
N (member #)	12	8	6
l_p^0	$\frac{\sqrt{2}a_0}{4}$	$\frac{\sqrt{3}a_0}{4}$	$\frac{a_0}{2}$
α_N	$\frac{\sqrt{2}I_{p}^{0.3}}{2}$	$\frac{4\sqrt{3}I_{p}^{03}}{2}$	$\frac{4I_{p}^{0.3}}{2}$
$v_s^0 = N\alpha_N$	$\frac{\frac{\sqrt{2}a_0}{4}}{\frac{\sqrt{2}l_p^{03}}{3}}$ $\frac{\frac{a_0^3}{4} \text{ or } 4\sqrt{2}l_p^{03}$	$\frac{a_0^3}{\frac{2}{2}}$ or $\frac{32\sqrt{3}}{9}l_p^{03}$ $\frac{8}{3}\delta_{ij}$	$\frac{\frac{a_0}{2}}{\frac{4l_p^{0^3}}{3}}$ $a_0^3 \text{ or } 8l_p^{0^3}$
$\sum_{I=1}^{N} n_i^I n_j^I$	$4\delta_{ij}$	$\frac{8}{3}\delta_{ij}$	$2\delta_{ii}$
$\sum_{I=1}^{N} n_i^I n_j^I n_k^I n_l^I$	$(1-\delta_{IK})\delta_{ij}\delta_{kl} + 2I_{ijkl}$	$\frac{8}{9} \left[(1 - 2\delta_{IK})\delta_{ij}\delta_{kl} + 2I_{ijkl} \right]$	$2\delta_{IK}\delta_{ij}\delta_{kl}$
c_{11}	$\frac{\lambda V_{,\lambda\lambda} + V_{,\lambda}}{4\sqrt{2}l_{-}^{03}}$	$\frac{\lambda V_{,\lambda\lambda} + 2V_{,\lambda}}{8\sqrt{3}I_0^{0.3}}$	$\frac{AV_{,\lambda\lambda}}{8I_0^{0.3}}$
c_{12}	$\frac{\lambda V_{,\lambda\lambda} - 5V_{,\lambda}}{8\sqrt{2}I^{0.3}}$	$\frac{\lambda V_{\lambda\lambda} - 4V_{\lambda}}{8\sqrt{3}I^{0.3}}$ $\frac{\lambda V_{\lambda\lambda} + 2V_{\lambda}}{8\sqrt{3}I^{0.3}}$	$-\frac{V_{,\lambda}}{8l^{0.3}}$
c_{44}	$\frac{\lambda V_{,\lambda\lambda} + 3V_{,\lambda}}{2\sqrt{2}v^3}$	$\frac{\lambda V_{,\lambda\lambda} + 2V_{,\lambda}}{2\sqrt{2} \ln^3}$	$\frac{V_{,\lambda}}{90^3}$
$K = \frac{\lambda V_{,\lambda\lambda} - 2V_{,\lambda}}{18\alpha_N}$	$\begin{array}{c} \lambda V_{,j,1} + V_{,1} \\ 4 \sqrt{2} p^3 \\ \lambda V_{,j,1} - 5 V_{,j} \\ 8 \sqrt{2} p^3 \\ \lambda V_{,j,2} + 5 V_{,j} \\ 8 \sqrt{2} p^3 \\ \lambda V_{,j,2} - 2 V_{,j} \\ 6 \sqrt{2} p^3 \end{array}$	$\frac{8\sqrt{3}I_{p}^{03}}{\lambda V_{,\lambda \lambda} - 2V_{,\lambda}} \frac{8\sqrt{3}I^{03}}{8\sqrt{3}I^{03}}$	$\begin{array}{c} 2\delta_{IK}\delta_{ij}\delta_{kl} \\ \frac{\lambda V_{,i,k}}{8lp^3} \\ -\frac{V_{,\lambda}}{8lp^3} \\ \frac{V_{,i}}{8lp^3} \\ \frac{\lambda V_{,i,k}-2V_{,\lambda}}{24lp^3} \end{array}$
Identity	$2c_{11} = c_{12} + 3c_{44}$	$c_{11} = c_{44}$	$c_{12} = -c_{44}$

Considering the relationship between the variations of average stress and average strain in Eq. (15) use the volume of singum $v_s = 4\sqrt{2}(\lambda l_p^0)^3$, one can obtain the stiffness tensor of the singum as

$$C_{ijkl} = \frac{(\lambda V_{,\lambda\lambda} - 5V_{,\lambda})\delta_{ij}\delta_{kl} - (\lambda V_{,\lambda\lambda} - V_{,\lambda})\delta_{IK}\delta_{ij}\delta_{kl} + 2(\lambda V_{,\lambda\lambda} + 3V_{,\lambda})I_{ijkl}}{8\sqrt{2}(l_p^0)^3}$$

$$(16)$$

which exhibits a cubic symmetry depending on the interatomic potential function and the geometry of the lattice or singum. The three independent elastic constants for the cubic symmetric lattice can be written as [41]:

$$c_{11} = \frac{\lambda V_{,\lambda\lambda} + V_{,\lambda}}{4\sqrt{2}l_{n}^{03}}, \quad c_{12} = \frac{\lambda V_{,\lambda\lambda} - 5V_{,\lambda}}{8\sqrt{2}l_{n}^{03}}, \quad c_{44} = \frac{\lambda V_{,\lambda\lambda} + 3V_{,\lambda}}{8\sqrt{2}l_{n}^{03}}$$
(17)

where the Voigt notation is used as $c_{11} = C_{1111}$, $c_{12} = C_{1122}$, and $c_{44} = C_{1212}$. The bulk modulus can be obtained as $K = (c_{11} + 2c_{12})/3$.

2.2. The singum model for general cubic lattices

The FCC singum model can be straightforwardly extended to other cubic lattices in the same fashion for BCC and SC lattices. In Fig. 3(a) of the BCC lattice, Node 0 has 8 closest neighbors. By cutting the bond length at its midpoint, a truncated octahedral singum can be obtained; whereas in Fig. 3(b) of the SC lattice, the singum shares the same shape and size as the cubic unit cell. Following the singum construction procedure in Eqs. (2)–(17), one can calculate the variables and list the in Table 1. Because the three lattices exhibit different packing efficiency, a new parameter of $\alpha_N=v_s^0/N$ is introduced as a measurement of the packing efficiency.

Mathematically, three independent elastic constants of c_{11} , c_{12} and c_{44} exist for solids with the cubic symmetry. However, the prediction

(15)

of them in Table 1 depends on only two quantities of $V_{,\lambda}$ and $V_{,\lambda\lambda}$ for each type of cubic lattice. Therefore, the three elastic constants are not truly independent for the cubic lattices with short-range interactions, but satisfy the identities shown in the last line of Table 1 [39].

At $I_p = I_p^0$ or $\lambda = 1$, $V_{,\lambda}(\lambda) = 0$. The SC lattice exhibits $c_{12}^{SC} = c_{44}^{SC} = 0$, which is physical because such a lattice structure is loose and cannot resist the shear load. When a prestress is considered with a boundary layer, it will generate a configurational stress [39,45] with the displacement variation and then contribute to the stiffness. For example, one can conduct an imaginary experiment with an SC lattice packaged by a membrane of the boundary layer. When the membrane is in a natural state without tension at $I_p = I_p^0$, the SC exhibits zero shear moduli; when the outside pressure is lower down, the membrane will expand like a balloon, and it will be able to resist a certain shear load; when the outside pressure increases, the lattice is compressed by the pressure and the SC is highly unstable, and a tiny shear strain may cause the collapse of the lattice unless opposite shear stress is applied for the equilibrium, which is corresponding to a negative shear modulus.

Given a lattice configuration and the corresponding bond potential, the singum model can predict the three elastic constants from Table 1. In the following, cellular materials with linear spring bonds and granular materials with Hertz's contacts are demonstrated with bond potentials that can be physically characterized.

3. Prediction of elasticity for cellular and granular lattices

The bond potential can be physically measured for cellular and granular lattices. Here we assume the bonds in the cellular lattices are connected by hinges so that the force will be along the bonds. Similarly, the granular lattices are packed with smooth spheres of equal diameters, so that the force will be along the center-center line of any pairs of contacted balls. The springs or balls are linear elastic so that the bond potential can be explicitly provided by the elastic constants of the springs or balls in cubic lattices.

3.1. Elastic behavior of cellular lattices with cubic structure

For linear elastic fibers in a cubic lattice, the potential function can be written as [39]:

$$V(r) = \frac{k}{2}(r - 2l_p^0)^2 \tag{18}$$

where k can be the spring coefficient of the fiber bond with the original length at $2l_n^0$. It can be rewritten in terms of the stretch ratio λ as:

$$V(\lambda) = 2k(l_n^0)^2 (\lambda - 1)^2$$
 (19)

Given Young's modulus E and cross-sectional area A at the stress-free state of the fibers, one can write

$$k = \frac{EA}{2I_n^0} \tag{20}$$

with $l_n^0 \gg \sqrt{A}$. The derivatives of $V(\lambda)$ can be written as

$$V_{\lambda}(\lambda) = 4k(l_n^0)^2(\lambda - 1)$$
 and $V_{\lambda\lambda}(\lambda) = 4k(l_n^0)^2$ (21)

which provides the effective elastic constants for FCC, BCC and SC, respectively, as follows:

$$c_{11} = k \frac{2\lambda - 1}{\sqrt{2} I_p^0}; \quad k \frac{3\lambda - 2}{2\sqrt{3} I_p^0}; \quad \frac{k\lambda}{2I_p^0}$$

$$c_{12} = k \frac{5 - 4\lambda}{2\sqrt{2} I_p^0}; \quad k \frac{4 - 3\lambda}{2\sqrt{3} I_p^0}; \quad \frac{k(1 - \lambda)}{2I_p^0}$$

$$c_{44} = k \frac{4\lambda - 3}{2\sqrt{2} I_p^0}; \quad k \frac{3\lambda - 2}{2\sqrt{3} I_p^0}; \quad \frac{k(\lambda - 1)}{2I_p^0}$$
(22)

$$K = k \frac{2(2-\lambda)}{3\sqrt{2}I_p^0}; \quad k \frac{2-\lambda}{2\sqrt{3}I_p^0}; \quad \frac{k(2-\lambda)}{6I_p^0}$$

where, by using Eq. (20), the parameter k/l_n^0 can be written as

$$\frac{k}{l_p^0} = \frac{EAl_p^0}{2(l_p^0)^3} = \frac{EM}{2\rho(l_p^0)^3} = \frac{E\overline{\rho}v_s}{2N\rho(l_p^0)^3} = \frac{E\alpha_N}{2\rho(l_p^0)^3}\overline{\rho}$$
(23)

in which M and ρ denote the mass and density of the fiber with the length l_p^0 ; $\overline{\rho}$ is the effective density of the cubic lattice; α_N depends on the number of the closest neighbor nodes at N=12,8 and 6 for FCC, BCC, and SC, respectively at

$$\alpha_N = \frac{\sqrt{2}l_p^{03}}{3}; \quad \frac{4\sqrt{3}l_p^{03}}{9}; \quad \frac{4l_p^{03}}{3}$$
 (24)

which can be found in Table 1 as well. Given a fiber type for a certain cubic structure, $\frac{E\alpha_N}{2\rho(l_p^0)^3}$ is a constant so that the stiffness is proportional to the effective density $\overline{\rho}$ at a certain stretch ratio λ .

3.2. Elastic behavior of granular materials with cubic structure

When many spherical elastic balls with the same diameter are packed in a cubic lattice, the force transfer through the contacts can be modeled with Hertz's contact [46]. If the balls are not smooth, the frictional force between the balls may be induced along the contacting surface [47]. However, for simplicity, this paper assumes the balls are smooth, so only normal forces are induced at the contact. Similarly to the 2D problem [40], Hertz's contact model provides the corresponding mutual approach of the two centers as [48]:

$$\delta = 2 \left[\frac{9P^2(1 - v^2)^2}{16E^2 l_p^0} \right]^{1/3} = 2(l_p^0 - l_p)$$
 (25)

or

$$P = 4\gamma I_p^{0^2} (1 - \lambda)^{3/2} \quad \text{with} \quad \gamma = \frac{E}{3(1 - v^2)}$$
 (26)

from which the potential function $V(\lambda)$ can be derived as

$$V = -\int_{r^0}^{r} P(r)dr = -2l_p^0 \int_{1}^{\lambda} P(\lambda)d\lambda = \frac{16}{5} \gamma (l_p^0)^3 (1-\lambda)^{\frac{5}{2}}$$
 (27)

in which $r^0=2l_p^0$ and $r=2l_p^0\lambda$ are used. The derivatives of $V_{,\lambda}(\lambda)$ and $V_{,\lambda\lambda}(\lambda)$ are written as below:

$$V_{,\lambda}(\lambda) = -8\gamma (l_p^0)^3 (1-\lambda)^{\frac{3}{2}}, V_{,\lambda\lambda}(\lambda) = 12\gamma (l_p^0)^3 (1-\lambda)^{\frac{1}{2}}$$
 (28)

which provides the effective elastic constants for FCC, BCC, and SC, respectively, as follows:

$$c_{11} = \frac{\gamma(1-\lambda)^{\frac{1}{2}}(5\lambda-2)}{\sqrt{2}}; \quad \frac{\gamma(1-\lambda)^{\frac{1}{2}}(7\lambda-4)}{2\sqrt{3}}; \quad \frac{3\gamma\lambda(1-\lambda)^{\frac{1}{2}}}{2}$$

$$c_{12} = \frac{\gamma(1-\lambda)^{\frac{1}{2}}(10-7\lambda)}{2\sqrt{2}}; \quad \frac{\gamma(1-\lambda)^{\frac{1}{2}}(8-5\lambda)}{2\sqrt{3}}; \quad \gamma(1-\lambda)^{\frac{3}{2}}$$

$$c_{44} = \frac{3\gamma(1-\lambda)^{\frac{1}{2}}(3\lambda-2)}{2\sqrt{2}}; \quad \frac{\gamma(1-\lambda)^{\frac{1}{2}}(7\lambda-4)}{2\sqrt{3}}; \quad -\gamma(1-\lambda)^{\frac{3}{2}}$$

$$K = \frac{\sqrt{2}\gamma(1-\lambda)^{\frac{1}{2}}(4-\lambda)}{3}; \quad \frac{\gamma(1-\lambda)^{\frac{1}{2}}(4-\lambda)}{2\sqrt{3}}; \quad \frac{\gamma(1-\lambda)^{\frac{1}{2}}(4-\lambda)}{6}$$

Note that given the material properties of the balls and the cubic lattice type of the granular lattice, because the size of the singum is defined by the radius of the balls as well, the effective density of the granular lattice with identical balls is independent of the ball radius, but inversely proportional to the packing efficiency. Therefore, the effective elasticity of the granular lattices is independent of the ball size as well.

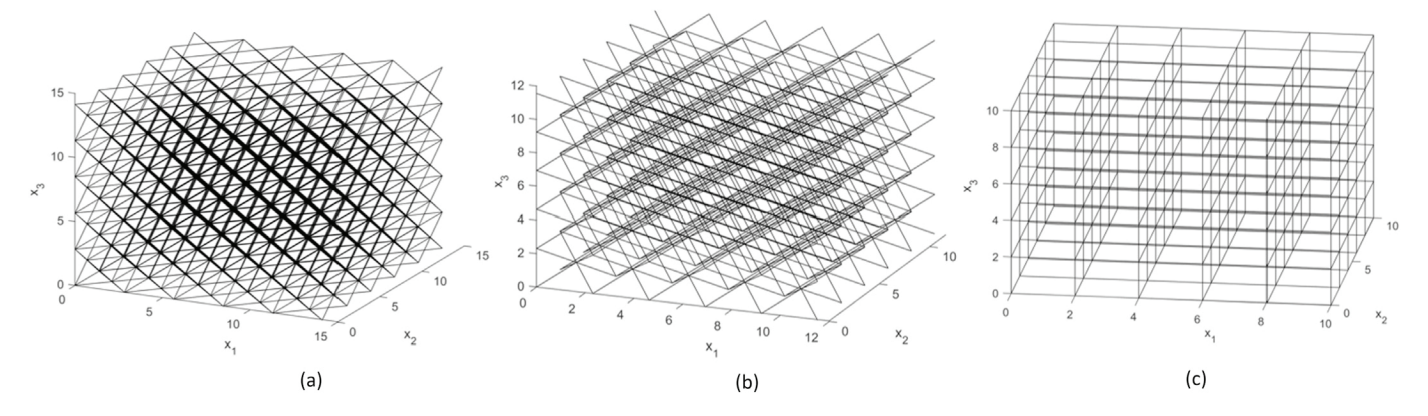


Fig. 4. The cubic lattice with $5 \times 5 \times 5$ unit cells for: (a) FCC lattice; (b) BCC lattice; (c) SC lattice.

3.3. Elastic behavior of randomly oriented cubic lattices

In engineering applications, some defects may easily distort the lattice in such a fashion that although on the microscale the material still exhibits cubic symmetry, on the macroscale the orientation of the local cubes varies randomly, which leads to an isotropic symmetry with two independent elastic constants, such as Young's modulus and Poisson's ratio. Consider the randomness of the cube's orientation, an orientational average [49,50] is applied to Eq. (14), the anisotropic terms will be averaged out, so that one can obtain isotropic elasticity.

Note that for a cubic symmetric elastic tensor with three independent elastic constants of c_{11} , c_{12} and c_{44} , by applying the orientational average on the elastic tensor, one can also obtain the isotropic elastic tensor with two independent parameters [38]:

$$K = \frac{c_{11} + 2c_{12}}{3} = \frac{\lambda V_{,\lambda\lambda} - 2V_{,\lambda}}{18\alpha_N}, \mu = \frac{c_{11} - c_{12} + 3c_{44}}{5} = \frac{\lambda V_{,\lambda\lambda} + 4V_{,\lambda}}{30\alpha_N}$$
 (30)

For cellular and granular lattices, using Eqs. (21) and (28), one can rewrite them explicitly as:

$$K^{cell} = \frac{2k(l_p^0)^2(2-\lambda)}{9\alpha_N}, \mu^{cell} = \frac{2k(l_p^0)^2(5\lambda - 4)}{15\alpha_N}$$
(31)

and

$$K^{gran} = \frac{2\gamma (l_p^0)^3 (1-\lambda)^{\frac{1}{2}} (4-\lambda)}{9\alpha_{N}}, \mu^{gran} = \frac{2}{15} \frac{\gamma (l_p^0)^3 (1-\lambda)^{\frac{1}{2}} (11\lambda - 8)}{\alpha_{N}}$$
(32)

Therefore, all isotropic elastic constants, such as Young's modulus and Poisson's ratio, can be calculated [20], respectively, as follows:

$$E = \frac{9K\mu}{3K+\mu} \quad \text{and} \quad v = \frac{3K-2\mu}{2(3K+\mu)}$$
 (33)

Particularly, Poisson's ratio for the cellular and granular lattices can be explicitly written as:

$$E^{cell} = \frac{k(l_p^0)^2 (2 - \lambda)(5\lambda - 4)}{3\alpha_N}, v^{cell} = \frac{6 - 5\lambda}{4}$$
 (34)

and

$$E^{gran} = \frac{\gamma (l_p^0)^3 (1 - \lambda)^{\frac{1}{2}} (4 - \lambda) (11\lambda - 8)}{3(2 + \lambda)\alpha_N}, v^{gran} = \frac{3(4 - 3\lambda)}{4(2 + \lambda)}$$
(35)

where the Poisson's ratio is 0.25 at $\lambda = 1$ and decreases with λ .

4. Verification of the singum model with the numerical simulation

The elastic constants can be verified with the structural analysis with lattices containing periodically distributed singums by applying a displacement load on the boundary [40]. A MATLAB code is developed to

verify the singum model prediction of elasticity compared to the numerical simulation.

4.1. Numerical simulation algorithm and implementation

The algorithm is structured and implemented as follows:

- 1. Initialize the simulation box by periodically extending the singum along x_1 , x_2 , x_3 direction with N_1 , N_2 , N_3 replications. The surfaces of the box are made of loading boards as a boundary layer. The node on the boundary is connected to them. The initial bond length and force are at $r = 2l_p^0$ and $\mathbf{F}^I = 0$, respectively, so $\lambda = 1$.
- 2. Given a testing mode, such as tension or shearing, apply the corresponding uniform Displacement Gradient (DG) $\delta d_{ij} = 10^{-6}$ to the box according to the Cauchy-Born's rule. The new positions of all nodes and cutting points are updated with Eq. (5).
- 3. Calculate the length change of each fiber and λ , and use the potential function $V(\lambda)$ to calculate the bond force. For each loading board, collect all bond forces and calculate the effective stress vector on each board with the deformed surface area. Using the effective stress vector on the 6 surfaces, one can obtain the stress variation caused by $\delta d_{ij}=10^{-6}$ at $\lambda=1$, and thus calculate the elastic tensor.
- 4. For any stretch ratio, namely λ^i , the coordinate of each node and the force in each bond can be calculated with Eq. (3). Repeat Steps 2 and 3 to calculate the elastic tensor at λ^i . Therefore, the relation of elastic tensor and λ can be calculated.

The above numerical simulation can be used for any type of potential, including the harmonic or Hertz's contact potential. In the following, we use the cellular lattices to demonstrate the implementation of the numerical simulation.

A unit cell with a center node and its members is used to construct the lattice structure. For instance, a $5 \times 5 \times 5$ FCC lattice contains 5 unit cells along x_1 , x_2 , x_3 directions, will have 666 nodes. Fig. 4 shows the three types of lattice structures but the actual simulations use much more unit cells in each direction.

After applying a uniform DG, following the procedures we described above, and repeating them until each node reaches equilibrium, the whole system will have a converged result after every node is balanced. For the central symmetric lattice, the equilibrium is guaranteed in one step following the Cauchy-Born rule [43].

Once all internal nodes are in equilibrium, one can collect the external forces on each loading board. Comparing them with the initial forces on each loading board, one can obtain the stress variation caused by the DG variation, and thus obtain the elastic modulus at the current configuration state and compare it with the predictions from the singum model.

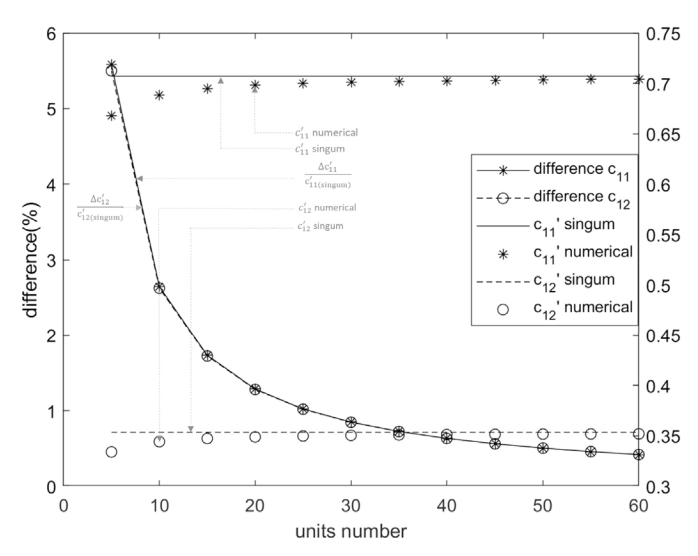


Fig. 5. The comparison between the singum model and numerical simulation with the varying number of the unit cells for the FCC lattice of the normalized elastic constants c_{11}' and c_{44}' at $\lambda=1$.

In the following case study, we assume an FCC lattice with spring coefficient $k = 10^6$ N/m and $\lambda = 1$. By applying a displacement gradient $\delta d_{11} = 10^{-6}$, the stress variation $\delta \sigma_{ij}$ can be obtained. Here we use an error threshold equal to 10^{-9} for the numerical simulations. From $\delta \sigma_{ij}$, the corresponding components of the stiffness tensor can be computed through $C_{ij11}=\delta\sigma_{ij}/\delta\varepsilon_{11}$ ($\delta\varepsilon_{11}=\lambda^{-2}\delta d_{11}$), and can be compared with the singum model's predictions. Note that in the simulation box, several nodes are on the boundary of the planes, like on the edges, so a discrepancy exists between the numerical results and the singum results. However, the difference reduces with the increase in the number of unit cells. Fig. 5 shows the numerical simulation results compared with the singum model results for different sizes from $5 \times 5 \times 5$ to $60 \times 60 \times 60$. Here the normalized stiffness tensor **C** by a factor of l_n^0/k is used as $c_{11}^{'}=c_{11}l_p^0/k$, $c_{12}^{'}=c_{12}l_p^0/k$, $c_{44}^{'}=c_{44}l_p^0/k$, and $K^{\prime}=Kl_p^0/k$. Therefore, one can eliminate the influence of k and l_p^0 and obtain a dimensionless stiffness for the comparison between numerical simulation and singum model prediction.

The numerical results are getting closer to the singum model's predictions when the size increases, which is because the singum model provides the exact solutions under small strain while the numerical results exhibit the boundary effect as we mentioned. When the FCC lattice increases its size from $5\times5\times5$ to $60\times60\times60$, the relative difference reduces from 5.6% to <0.5% for c'_{11} and c'_{12} at the similar convergent rate although their values are fairly different as shown in Fig. 5.

The boundary effect has different influences for the three different types of lattice. To guarantee accurate results from the numerical simulation, $30 \times 30 \times 30$ or more unit cells are used to minimize the boundary effect, which exhibits an error less than 1% in Fig. 5.

4.2. Verification of elastic constants for cellular lattices

When a large number of unit cells are used, the effective stiffness calculated from the numerical simulation converges to the unique value for an infinite large lattice, which shows the exactness of the singum model at $\lambda=1$ in Fig. 5. When the cubic lattices are under hydrostatic stress, λ changes with the stress states. The singum model predicts the tangential stiffness tensor, whose exactness can also be demonstrated as follows:

Fig. 6 demonstrates the comparisons between the singum prediction and numerical simulation for three cellular lattices, in which $30\times30\times30$ unit cells are simulated for FCC and SC cellular lattices and $80\times80\times80$ unit cells are used for BCC simulations. Excellent agreement between

the numerical simulation and the singum formulation in Eq. (22), which shows that the singum model indeed provides the exact solution. Note that although we focus on tensile loading for cellular lattices physically, here a larger range of $\lambda \in (0.6,2)$ is illustrated including a compressive range. The following features are highlighted for the effective elasticity changing with λ :

- 1. The normalized elastic moduli c'_{11} and c'_{44} increases with λ ; whereas c'_{12} and K' decrease with λ .
- 2. When an elastic constant is zero or negative, the solid generally becomes unstable and may collapse or break down. However, it is not caused by buckling or fracture of the bonds but by configurational stress, so that the negative elastic constant still exhibits a physical meaning. For example, when λ is small than 1, c'_{44} can reach negative first, at which a shear strain variation may produce a moment requiring an opposite shear stress to balance the lattice, which is obvious for SC lattices. When λ is large, an increase of the volumetric strain may cause the reduction of the stress by the increased surface area and thus leads to a negative bulk modulus.
- 3. The three lattices exhibit different patterns of the elastic constant variations with λ : c'_{11} and c'_{44} are parallel to each other but overlapped for BCC.
- 4. Because c'_{11} , c'_{12} , and K' are not independent from each other, when $c'_{11} = c'_{12}$, K' shall be the same as them. Therefore, they share an intersection point for FCC, BCC, and SC lattices at $(7/8, 3\sqrt{2}/8)$, $(1, \sqrt{3}/6)$, and (0.5, 0.25) projected, respectively.

Although the spring coefficient is a constant, the effective stiffness of the lattice is not a constant anymore but linearly changes with λ . When the bond potential is not harmonic for granular lattices, the effective stiffness can also be analytically predicted as follows.

4.3. Verification of elastic constants for granular lattices

Similarly, the granular lattices can be well simulated when applying the Hertz contact potential. The effective stiffness tensor can be normalized by γ as: $c_{11}^{'}=c_{11}/\gamma$, $c_{12}^{'}=c_{12}/\gamma$ and $c_{44}^{'}=c_{44}/\gamma$. The bulk modulus K can be normalized as $K'=K/\gamma$ as well. $30\times30\times30$ simulation box is used for FCC granular lattice, and $80\times80\times80$ simulation box is used for SC and BCC to achieve well-convergent results. Although Hertz's contact is typically applicable to the infinitesimal deformation, $\lambda \in (0.8,1)$ is used to compute corresponding stiffness tensor values and bulk modulus

The singum model shows high consistency predictions for granular lattices too. Its predictions excellently agree with the numerical simulation results, which show the exactness of the singum model. The following features can be observed in Fig. 7:

- 1. When $\lambda=1$, all the elastic moduli become zero. The phenomena can be understood physically: without any prestress applied to the granular structure, the contacts between each node are not established at all. All the granular units are just simply stacked together and there are no forces to hold them. If applied prestress to the granular structure, contacts can transform the forces into each other, and such interactions provide stiffness for the whole structure.
- 2. When $\lambda < 1$ but close to 1, except c_{44}' for the SC lattice, all other elastic moduli for the three cubic lattices nonlinearly increase from zero to positive values, which is different from the cellular lattices in Fig. 6. Here the four elastic moduli linearly change with λ as c_{11}' and c_{44}' monotonically increase while c_{12}' and K' monotonically decrease.
- 3. Essentially, the elastic moduli are polynomial functions of $1-\lambda$; c_{12}' and K' decreases with λ so they are positive under compression; and c_{11}' and c_{44}' shows strong nonlinear behavior with the maximum values can be found between 1 and 0.5 for λ .

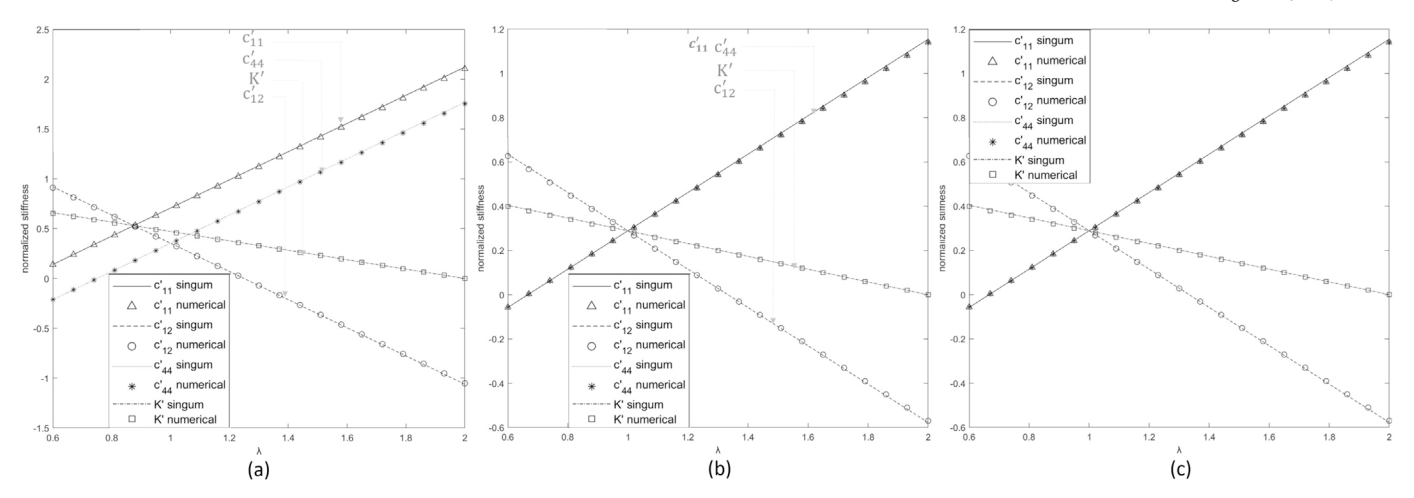


Fig. 6. Comparison of normalized elastic constants between the singum model and numerical simulation for (a) FCC, (b) BCC, and (c) SC cellular lattices.

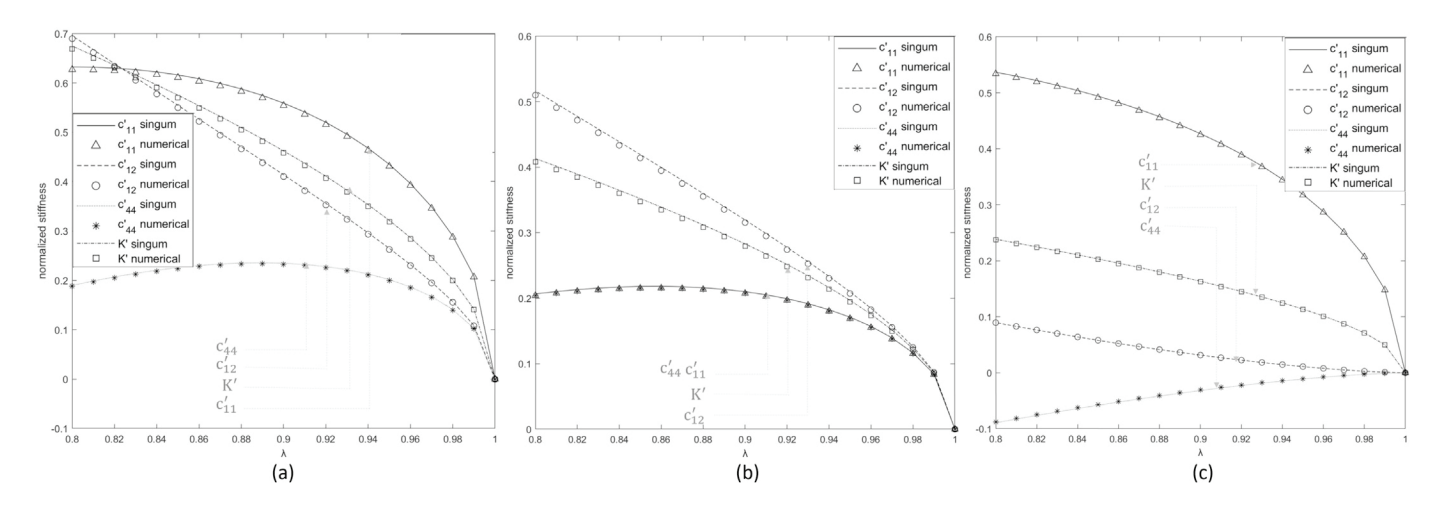


Fig. 7. Comparison of normalized elastic constants between the singum model and numerical simulation for (a) FCC, (b) BCC, and (c) SC granular lattices.

4. Similarly to the cellular lattices, c'_{11} , c'_{12} and K' share the same intersection at (0.824, 0.629) and (0.4, 0.465) for FCC and SC; whereas they do not have any intersection other than (0,0) for BCC.

Note that Hertz's contact area and the center-center distance change with the compression force nonlinearly, and the stress distribution is not uniform, which causes material yielding at a relatively small force. Moreover, multiple contact points on one ball may change the potential function as well. The present formulation based on Hertz's contact model requires experimental validation and may only apply to a very small range of λ .

5. Results and discussion

As verified by the numerical simulation, the singum model provides the exact prediction of elasticity for the cubic lattice materials with potential-based bonds. It can be applied in lattice material design and analysis. Without loss of any generality, aluminum fibers or balls are chosen for material design with the following material constants [41, 51] at the room temperature and atmospheric pressure:

Young's modulus E=69 Gpa; Density $\rho=2.710\times 10^3$ Kg/m³; Bulk modulus K=76.3 GPa; Poisson's ratio $\nu=0.33$; Thermal expansion coefficient $\alpha=23.4\times 10^{-6}$ °C⁻¹.

The lattice materials are packaged by a boundary layer of different materials for different designs. Although aluminum typically yields at about 300 MPa, this paper will consider the linear elastic behavior only for simplicity, but the plastic deformation should be carefully addressed

in the actual applications. The method or results can be generalized to other materials in the same way by replacing the above material constants. To study the effect of the prestress, the lattice is packaged by a boundary layer, which is similar to the loading board in the numerical simulation and can provide confining stress when a prestress is applied. The aluminum fiber diameter is 0.5 mm and the ball diameter is 10 mm, unless they are specifically changed for parametric studies.

5.1. Effects of singum size or effective density at $\lambda = 1$

Given the fiber diameter, the effective density of the cellular lattice changes with the singum size of l_p^0 and the lattice types. c_{11} , c_{12} , c_{44} and K for different cellular lattices are computed and compared in Fig. 8(a):

- 1. When l_p^0 decreases, stiffness tensor elements, and K value increase. It is because when l_p^0 decreases, the effective density increases accordingly. The similar phenomena can be seen in Fig. 9 for E, K, and μ as well.
- 2. When no prestress is applied, $\lambda=1$ and $V_{,\lambda}=0$, so c_{11} , c_{12} and c_{44} only depend on $V_{,\lambda\lambda}$, c_{12} and c_{44} share the same value for SC at zero, so they are not shown. The four curves for BCC overlap. The curves of c_{12} and c_{44} for FCC overlaps.
- 3. Given a value of l_p^0 , FCC exhibits the highest values of all four elastic moduli among the three lattices, but c_{11} of SC is higher than that of BCC, whereas K of BCC has a larger value than SC.

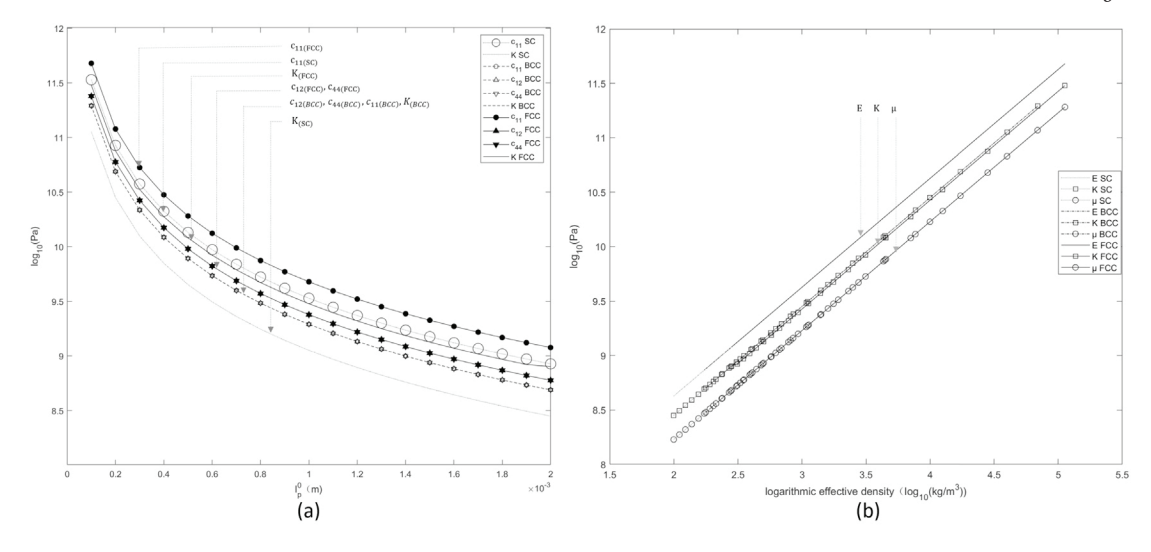


Fig. 8. Elastic moduli c_{11} , c_{12} , c_{44} and K versus l_p^0 for cellular FCC, BCC, and SC lattices, $c_{12(SC)}$ and $c_{44(SC)}$ are not shown as both are constant as zero (a). Elastic moduli E, K, and μ versus effective density for cellular FCC, BCC and SC lattices (b).

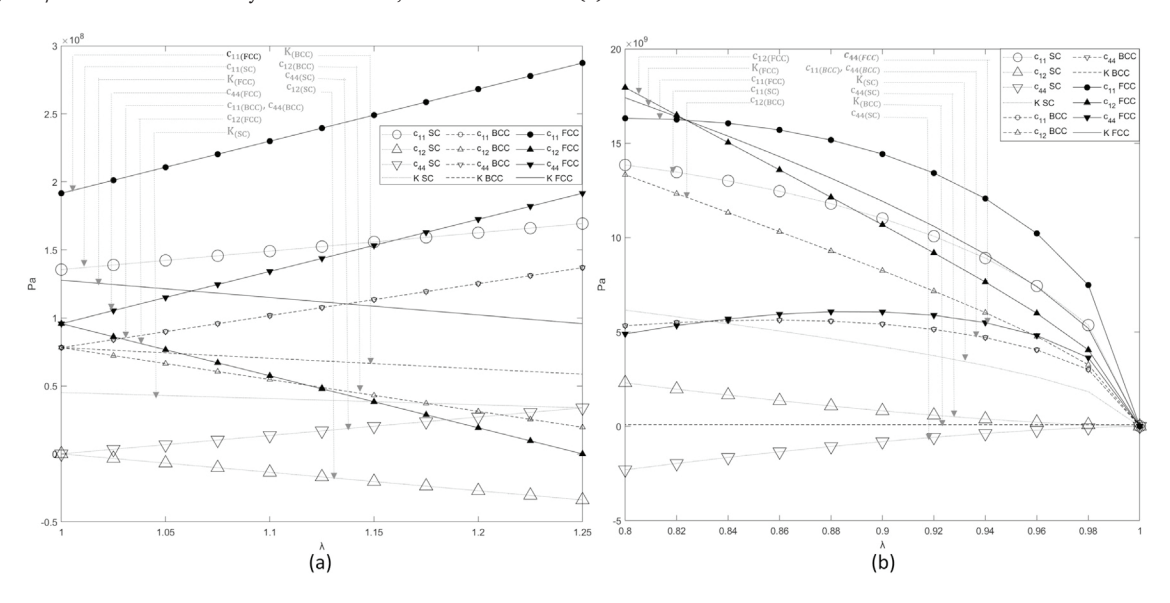


Fig. 9. Elastic moduli c_{11} , c_{12} , c_{44} and K versus λ for cellular FCC, BCC, and SC lattices (a) and granular lattices (b).

Note that the densities of FCC, BCC, and SC are in a decreasing order at the same I_p^0 . Obviously, c_{11} changing with the three lattices does not follow the trend of density, particularly for BCC and SC with different cubic symmetry.

When the orientation of the lattices randomly changes, using the orientational average, one can obtain the elastic modulus of E, K, and μ . Fig. 8(b) shows their variations with the density of the lattice with the following highlights:

- 1. When logarithmic relative density $log_{10}(\rho)$ increases, E, K and μ increase, as discussed for Fig. 8. Their variation is linear in the log scale, which is reasonable because the strain energy density will follow the density of the lattice as each bond is subjected to the same strain statistically with the orientational average.
- 2. E, K, and μ only depend on the relative density, no matter which lattice structure is used. In other words, with the orientational average, the anisotropic nature is lost, so that FCC, BCC, and SC exhibit the same isotropic properties in terms of the lattice effective density as follows:

$$K^{cell} = \frac{E(2-\lambda)}{9\rho}\overline{\rho}, \mu^{cell} = \frac{E(5\lambda-4)}{15\rho}\overline{\rho}$$
 (36)

which is obtained by Eqs. (31) and (23). Then one can calculate Young's modulus by Eq. (33) as

$$E^{cell} = \frac{E(2-\lambda)(5\lambda - 4)}{6\rho}\overline{\rho}$$
 (37)

3. The three elastic moduli exhibit $E > K > \mu$ as Eqs. (36) and (37) show $\mu = 0.6K$ and E = 1.5K, respectively, at $\lambda = 1$.

For granular lattice, when $\lambda=1$, c_{11} , c_{12} c_{44} and E, K, μ equal to 0, because contacts are not established as we mentioned in the last section, so the hertz potential and its derivatives are all equal to 0. For both cellular and granular lattices, when $\lambda=1$, Poisson's ratio $\nu\to0.25$, which is irrelevant to the lattice types as shown in the next section.

5.2. Effects of the prestress or λ at a given singum size

Although the bond materials are linear elastic for either springs or balls, the effective stiffness of the lattices change with λ or prestress in the bonds significantly. Here we fix $l_p^0=5$ mm and show the elastic moduli changing with λ for both cellular and granular lattices. Fig. 9(a) shows c_{11}, c_{12}, c_{44} and K for cellular lattices when λ changes from 1 to 1.25. Applying the method, we could study the λ changes on a larger

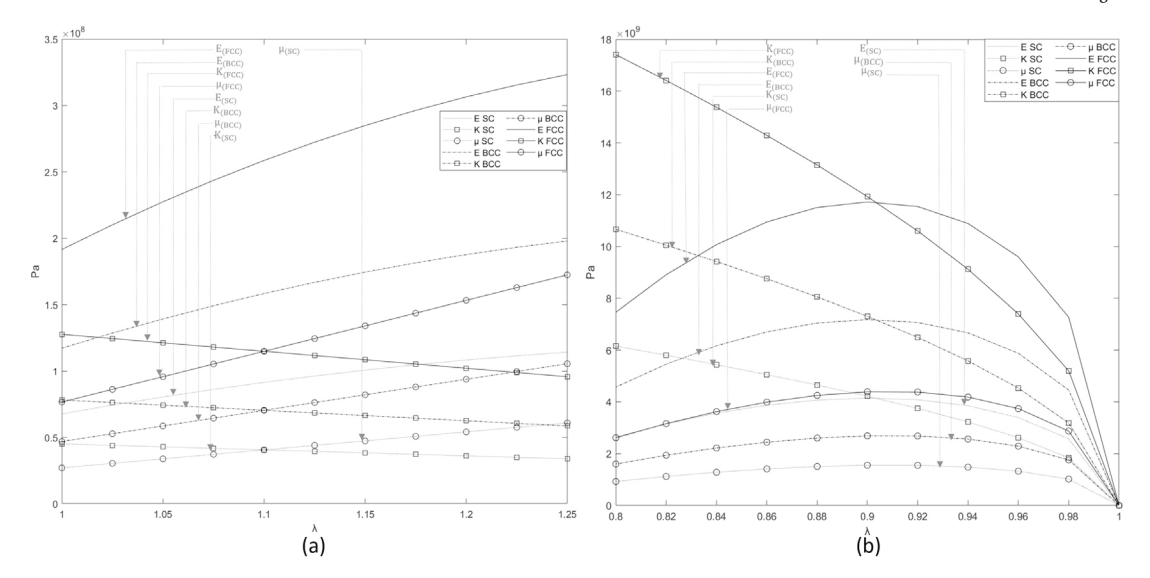


Fig. 10. Elastic moduli K, E and μ versus λ for cellular FCC, BCC, and SC lattices (a) and granular lattices (b).

scale, but consider if the pre-stress exceeds the material elastic limit, plastic deformation might exist on the lattice. Especially, for cellular materials, if the aspect ratio indicates bars are slender, then under a certain compression load, the bars will lose their stability and the local buckling effect might be observed as well. [52] These effects were out of the scope of this manuscript and not evaluated in results, so we plotted the graphics under a relatively small range of λ . For all three lattices, c_{11} and c_{44} increases; while c_{12} and K decreases with λ . However, different lattices show different changing rate. For example, although c_{12} of FCC is higher than that of BCC at $\lambda=1$, when $\lambda=1.15$, FCC exhibits a lower c_{12} .

Fig. 9(b) demonstrates the effective elastic moduli of granular lattices when λ changes from 0.8 to 1. The linear variation of the effective elastic moduli with λ in Fig. 9(a) does not exist for granular lattice anymore. All elastic moduli exhibit a value of zero at $\lambda=1$. In general, FCC shows higher elastic moduli than BCC, and then SC. However, SC provides a high value of c_{11} and a negative value of c_{44} in comparison with those for BCC.

When an orientational average is used, one can also obtain the variations of E, K and μ with λ for both cellular and granular lattices in Figs. 10(a) and 10(b) for cellular and granular lattices, respectively. In Fig. 10(a), although K and μ linearly change with λ , Young's modulus exhibits nonlinear trends for the three types of the cubic lattice. Again, the isotropic elastic moduli follow the density of the lattices, so that the elastic moduli for FCC, BCC and SC exhibit a decreasing order as their density decrease.

Similarly, Poisson's ratio can be determined as well when λ is given. Fig. 11 provides the results of Poisson's ratio changing with: $\lambda \in (0.8,1)$ for granular lattices and $\lambda \in (1,1.25)$ for cellular lattices, respectively. The three cubic lattices exhibit the same Poisson's ratio changing with λ , but the cellular lattices and granular lattices do not share the same trend, although they both provide $\nu = 0.25$ at $\lambda = 1$.

5.3. Effect of temperature on the thermoelasticity of packaged cubic lattices

As the singum model provides the exact solution of the effective stiffness of cubic lattices in terms of prestress or λ , it provides a powerful tool for material design with tailorable thermoelastic properties.

Similarly to our previous work for 2D granular lattices with a wrapping layer [40], this subsection provides a simple demonstration with a lattice-based material packaged by a spherical boundary layer with a prestress. Under the unstressed state, the aluminum lattice material forms a spherical domain with radius \mathbb{R}^l , and is packaged by a boundary layer of a membrane with Young's modulus \mathbb{E}^B , Poisson's ratio \mathbb{V}^B , ther-

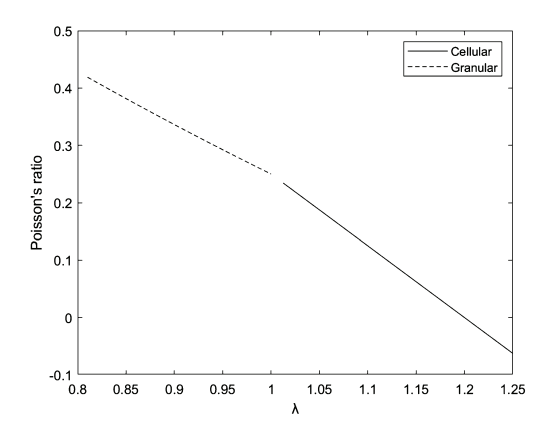


Fig. 11. Poisson's ratio versus λ for cellular lattices and granular lattices.

mal expansion coefficient α^B , thickness t, and inner radius R^i ($t \ll R^i$) at the room temperature. When $R^i \neq R^l$, a prestress of $\sigma = \sigma^m \delta_{ij}$ is required to make the lattice and boundary layer bounded to each other with a final radius $R \in (R^i, R^l)$. The membrane stress in the boundary layer can be calculated by the equilibrium of the semi-spherical sectional area:

$$\sigma^B = -\frac{\sigma^m \pi R^2}{2\pi Rt} = -\frac{\sigma^m R}{2t} \tag{38}$$

The bi-directional membrane stress is related to the membrane strain ε^B as:

$$\varepsilon^B = s\sigma^B = -\frac{s\sigma^m R}{2t} = \frac{R - R^i}{R} \tag{39}$$

where $s = \frac{1-v^B}{E^B}$ and Eq. (38) is used.

The hydrostatic stress of the lattice is related to the stretch ratio change as

$$\sigma^{m} = \int_{v_{s}^{0}}^{v_{s}} \frac{K(v_{s})}{v_{s}} dv_{s} = 3 \int_{1}^{\lambda} \frac{K(\lambda)}{\lambda} d\lambda$$
 (40)

where $K(\lambda)$ is given in the singum model by $V(\lambda)$ in Eq. (30) with $\lambda = R/R^l$. For cellular lattices, Eq. (40) can be rewritten as:

$$\sigma^{m} = \frac{2k(l_{p}^{0})^{2}(2\ln\lambda - \lambda + 1)}{3\alpha_{N}}$$
(41)

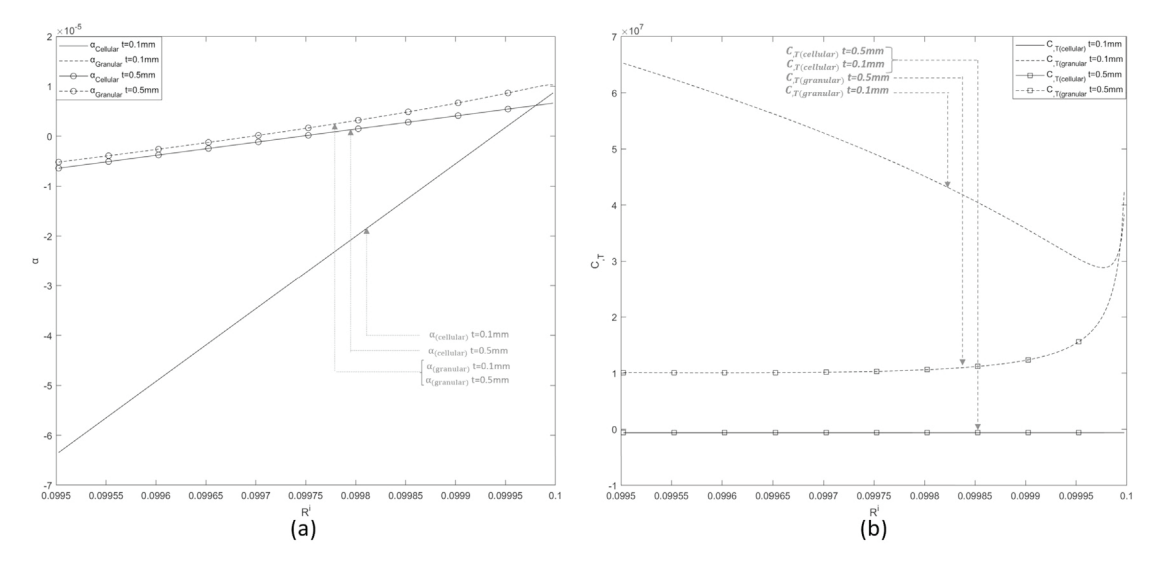


Fig. 12. FCC aluminum lattices packaged by a titanium boundary layer at t = 0.1 and 0.5 mm for (a) Effective thermal expansion coefficients α^{ball} (b) Effective temperature derivatives of Young's modulus (E_T^{ball}) .

Similarly, for granular lattices, one can obtain:

$$\sigma^{m} = \frac{2\gamma (l_{p}^{0})^{3} \left[8(1-\lambda)^{\frac{1}{2}} - 4\ln\frac{1+(1-\lambda)^{\frac{1}{2}}}{1-(1-\lambda)^{\frac{1}{2}}} + \frac{2(1-\lambda)^{\frac{3}{2}}}{3}\right]}{3\alpha_{N}}$$
(42)

Substituting Eq. (41) or (42) into Eq. (39) yields R as:

$$R = \frac{(4t^2 + 8stR^i\sigma^m)^{\frac{1}{2}} - 2t}{2s\sigma^m} \tag{43}$$

Therefore, given R^l , R^i , and t as well as the material elastic constants at room temperature T_0 , one can solve $R(T_0)$ and $\lambda(T_0)$ by the above equations. Note that Eq. (43) is an implicit equation as λ in σ^m depends on R as well. An iteration method can be used to solve for R as follows: First assume $R = (R^l + R^i)/2$ to calculate λ and σ^m and update R, and repeat the step until R is convergent. The stiffness of the lattice can be obtained based on $\lambda(T_0)$, namely, $\mathbf{C}(T_0)$.

When this composite ball is subjected to a temperature change δT , R^i , R^i , and t will be updated with the thermal expansion coefficient of the boundary layer and the lattice material at $T_1 = T_0 + \delta T$. The temperature derivative of the stiffness for aluminum and boundary layer is typically negative, a measurement value of the temperature derivative of aluminum's Young's modulus under room temperature (20 °C to 40 °C) is -0.1 GPa/°C [53], and for titanium, the temperature derivative of Young's modulus under room temperature (20 °C to 205 °C) is -0.054 GPa/°C with Young's modulus at room temperature at 110 GPa [54]. Here the Poisson's ratio is assumed to be constant. Reusing the above equations, one can solve $R(T_1)$ and $\lambda(T_1)$. The stiffness of the lattice can be updated with $\lambda(T_1)$ and new elasticity of the materials, namely, $\mathbf{C}(T_1)$.

Therefore, one can calculate the effective thermal expansion coefficient of the ball as

$$\alpha^{ball} = \frac{R(T_1) - R(T_0)}{R(T_0)\delta T} \tag{44}$$

and the thermal derivative of the elasticity can also be derived as

$$\mathbf{C}_{,T}^{ball} = \frac{\mathbf{C}(T_1) - \mathbf{C}(T_0)}{\delta T} \tag{45}$$

Using a small temperature change, namely $\delta T=1/^{\circ}\mathrm{C}$ or smaller, one can calculate the above values with convergent results. Obviously, α^{ball} and $\mathbf{C}_{,T}^{ball}$ depends on the design of R^{l} , R^{i} , and t once the lattice type and bond material is given. The above equations can be applicable to both the cubic and isotropic elasticity.

In the following, we demonstrate aluminum FCC cellular and granular lattices packaged by a titanium boundary layer with the following parameters: $R^l = 100$ mm, t = 0.1 or 0.5 mm, $R^i \in (99.5-100$ mm) for cellular and granular lattices. Fig. 12(a) and (b) provide the results for cellular and granular lattices, respectively, at t = 0.1 and 0.5 mm.

With the temperature increase, two mechanisms contribute to the effective thermoelastic behavior: First, because aluminum exhibits a larger negative temperature derivative of the Young's modulus, as the lattice core becomes softer, the tensile stress in the titanium will decrease, which leads to the reduction of the dimension of the ball. On the other hand, the thermal expansions of both lattice and boundary layer lead to the increase of the ball size. Therefore, effective thermal expansion is the combination of the two effects. The following features can be observed:

- 1. Negative α^{ball} obtained for both cellular and granular materials, and when R^i increases, α^{ball} increases as well.
- 2. When the thickness increases from 0.1 to 0.5 mm, α^{ball} for the granular core nearly overlaps with each other as the stiffness of the core is dominant; whereas for the cellular core, the small thickness yields a higher variation of α^{ball} .
- 3. For the thermal derivative of Young's modulus, granular lattices exhibit positive values at a smaller R^i and non-linearly change with R^i ; whereas cellular lattices show small changes with negative values
- 4. When the thickness increases from 0.1 to 0.5 mm, the temperature derivative of Young's modulus for the cellular core overlaps with each other; whereas the granular core produces a large difference.

The singum model provides a powerful tool to understand cellular and granular lattice, and their thermoelastic performances can be well predicted and tailored by the prestress. Although the concept of prestress has been commonly used in steel-reinforced concrete to shift the compressive and tensile stresses and thus increase the overall material strength, it has never been used to change the material's stiffness or thermoelasticity yet. The above study shows that the elastic and thermoelastic performance of the lattice-based materials can be altered by adjusting their prestress or λ , which creates a new way to fabricate ultra-lightweight smart materials and structures with pre-stressed lattice materials [8]. Particularly, in space applications, lightweight but stiff materials are needed to save propulsion energy in transportation, and stability under different temperature ranges is crucial to keep the integrity and shape of the materials and structures. The design of a

C. Liu and H. Yin Materials & Design 233 (2023) 112223

hierarchical lattice material with cellular balls for granular lattices can achieve nearly zero thermal expansion coefficient and temperature derivative of Young's modulus [9].

6. Conclusions

The singum model has been extended to 3 types of cubic lattices, namely FCC, BCC, and SC, for both cellular and granular materials with the harmonic potential and Hertz's contact potential for the bonds, respectively. A numerical method is developed to verify the singum model for all cases, which show that the singum model provides exact solutions for cubic lattice-based materials. Using the boundary layer, one can change the prestress in the bonds to tailor the effective elasticity, thermal expansion coefficient, and temperature derivative of elasticity of the lattice-based materials. The following conclusions are highlighted from the analysis:

- The cubic symmetric elasticity for FCC, BCC, and SC is formulated explicitly in terms of the potential of the bond and the lattice characteristics. The 3 cubic elastic constants are not fully independent but satisfy one identity for each type of cubic symmetry.
- 2. The elastic moduli change with the prestress or stretch ratio λ of the bonds due to the configurational stress: for the cellular lattices, c_{11} and c_{44} increase while c_{12} and K decrease with λ linearly; while for granular lattices, the elasticity shows strong nonlinearity with zero elasticity at $\lambda=1$.
- 3. When the lattice orientation randomly changes, the cubic lattice may exhibit isotropic elasticity, which is predicted by the orientational average of the cubic elasticity. The Poisson's ratio is 0.25 at $\lambda = 1$ for all cases. Under compression, it is higher than 0.25, while under tension it is lower than 0.25.
- 4. For cellular lattices, given the cross-sectional area of the bond material, the effective elasticity is proportional to the effective density of the lattices under the undeformed configuration.
- 5. Given the configuration of the lattice packaged by a boundary layer, the effective thermal expansion and temperature derivative of elasticity can be calculated, and are tailorable by the prestress that depends on the thickness of the boundary layer and initial mismatch between the lattice core and boundary layer.

Overall, the singum model interprets the fundamental mechanics and physics of cubic lattice-based materials and can be extended to other types of lattices. It provides a powerful tool for material design and analysis and creates a new way to fabricate ultra-lightweight smart materials and structures, which can achieve zero effective thermal expansion coefficient and temperature derivative of Young's modulus.

CRediT authorship contribution statement

Chao Liu: Data curation, Methodology, Software, Visualization, Writing – original draft. **Huiming Yin:** Conceptualization, Funding acquisition, Resources, Supervision, Writing – original draft, Writing – review & editing.

Declaration of competing interest

The authors declare that they have no known competing financial interests or personal relationships that could have appeared to influence the work reported in this paper.

Data availability

Data will be made available on request.

Acknowledgement

This work is sponsored by NASA SBIR #80NSSC22PB164 and NSF IIP #1738802 and #1941244. We thank Mr. Chuck Taylor and Mr. Richard Pappa from NASA for their support of the work. The authors thank Dr. Jeffrey Kysar and Dr. Sinan Keten for the helpful discussion and the sharing of their relevant work and Dr. Byung-Wook Kim for his artwork of the cubic lattices. This work was inspired by Dr. Richard Li's Ph.D. dissertation. In addition, we are grateful to Dr. Mehdi Zadshire and Mr. Frank Pao for the patent preparation.

References

- R. Lakes, Foam structures with a negative Poisson's ratio, Science 235 (1987) 1038–1041.
- [2] M.C. Boyce, E.M. Arruda, Constitutive models of rubber elasticity: a review, Rubber Chem. Technol. 73 (3) (2000) 504–523.
- [3] B.A. Davey, H.A. Priestley, Introduction to Lattices and Order, Cambridge University Press, 2002.
- [4] N. Shahrubudin, T.C. Lee, R. Ramlan, An overview on 3d printing technology: technological, materials, and applications, Proc. Manuf. 35 (2019) 1286–1296.
- [5] B.J. Sahariah, A. Namdeo, P. Khanikar, Composite-inspired multilattice metamaterial structure: an auxetic lattice design with improved strength and energy absorption, Mater. Today Commun. 30 (2022) 103159.
- [6] P. Wang, F. Yang, P. Li, B. Zheng, H. Fan, Design and additive manufacturing of a modified face-centered cubic lattice with enhanced energy absorption capability, Extreme Mech. Lett. 47 (2021) 101358.
- [7] L.-Y. Chen, S.-X. Liang, Y. Liu, L.-C. Zhang, Additive manufacturing of metallic lattice structures: unconstrained design, accurate fabrication, fascinated performances, and challenges, Mater. Sci. Eng., R Rep. 146 (2021) 100648.
- [8] C. Liu, J. Lou, F. Pao, H. Yin, M. Zadshir, Tailoring thermoelastic constants of cellular and lattice materials with pre-stress for lightweight structures, U.S. Patent App. 17/935,155, September 26, 2022.
- [9] C. Liu, F. Pao, H. Yin, M. Zadshir, Design and manufacture of a hierarchical latticebased material with ultra-lightweight, high stiffness, and designable thermoelasticity, US Patent Application 63/485,033, 2/15/2023, 2023.
- [10] M. Smith, D. Craig, N. Herrmann, E. Mahoney, J. Krezel, N. McIntyre, K. Goodliff, The Artemis program: an overview of NASA's activities to return humans to the Moon, in: 2020 IEEE Aerospace Conference, IEEE, 2020, pp. 1–10.
- [11] M. Zadshir, C. Liu, J. Lou, H. Yin, Advanced material and structural design of a lightweight stiff mounting system for a 50 kw-class photovoltaic array, Tech. rep., PVT Clearn Energy, LLC, NASA SBIR Phase I, Final Report, Award#: 80NSSC22PB164, 2023.
- [12] R. Pappa, G. Rose, D. Paddock, R. Lepsch, J. McNatt, J. Fincannon, Solar power for lunar pole missions, Space Power Workshop, no. NF1676L-32036, 2019.
- [13] N. Kumari, J.M. Bretzfelder, I. Ganesh, A. Lang, D.A. Kring, Surface conditions and resource accessibility at potential Artemis landing sites 007 and 011, Planet. Sci. J. 3 (9) (2022) 224.
- [14] Y. Jia, L. Liu, X. Wang, N. Guo, G. Wan, Selection of lunar south pole landing site based on constructing and analyzing fuzzy cognitive maps, Remote Sens. 14 (19) (2022) 4863.
- [15] H. Benaroya, Lunar habitats: a brief overview of issues and concepts, Reach 7 (2017) 14–33.
- [16] R.B. Malla, K.M. Brown, Determination of temperature variation on lunar surface and subsurface for habitat analysis and design, Acta Astronaut. 107 (2015) 196–207.
- [17] A. Šturcová, G.R. Davies, S.J. Eichhorn, Elastic modulus and stress-transfer properties of tunicate cellulose whiskers, Biomacromolecules 6 (2) (2005) 1055–1061.
- [18] T. Mura, Micromechanics of Defects in Solids, Springer Netherlands, 1987.
- [19] J.R. Willis, Mechanics of Composites, Ecole polytechnique, Département de mécanique, 2002.
- [20] H. Yin, Y. Zhao, Introduction to the Micromechanics of Composite Materials, CRC Press, 2016.
- [21] J. Ju, T. Chen, Micromechanics and effective moduli of elastic composites containing randomly dispersed ellipsoidal inhomogeneities, Acta Mech. 103 (1) (1994) 103–121.
- [22] C.L. Tucker III, E. Liang, Stiffness predictions for unidirectional short-fiber composites: review and evaluation, Compos. Sci. Technol. 59 (5) (1999) 655–671.
- [23] K. Li, X.-L. Gao, A. Roy, Micromechanics model for three-dimensional open-cell foams using a tetrakaidecahedral unit cell and Castigliano's second theorem, Compos. Sci. Technol. 63 (12) (2003) 1769–1781.
- [24] Y. Chen, F. Scarpa, Y. Liu, J. Leng, Elasticity of anti-tetrachiral anisotropic lattices, Int. J. Solids Struct. 50 (6) (2013) 996–1004.
- [25] S. Xu, J. Shen, S. Zhou, X. Huang, Y.M. Xie, Design of lattice structures with controlled anisotropy, Mater. Des. 93 (2016) 443–447.
- [26] Y. Gao, Z. Zhou, H. Hu, J. Xiong, New concept of carbon fiber reinforced composite 3d auxetic lattice structures based on stretching-dominated cells, Mech. Mater. 152 (2021) 103661.

- [27] J. Duffy, R. Mindlin, Stress-strain relations and vibrations of a granular medium, J. Appl. Mech. 24 (4) (1957) 585–593.
- [28] J. Duffy, A differential stress-strain relation for the hexagonal close-packed array of elastic spheres, J. Appl. Mech. 26 (1) (1959) 88–94.
- [29] H. Deresiewicz, Stress-strain relations for a simple model of a granular medium, J. Appl. Mech. 25 (3) (1958) 402–406.
- [30] H. Makhlouf, J. Stewart, Elastic constants of cubical-tetrahedral and tetragonal sphenoidal arrays of uniform spheres, in: Proc., Int. Symp. of Wave Propagation and Dynamic Properties of Earth Materials, 1967, pp. 825–837.
- [31] C. Chang, Micromechanical Modelling of Constitutive Relations for Granular Material, vol. 20, Elsevier, 1988, pp. 271–278.
- [32] S. Nadimi, T. Shire, J. Fonseca, Comparison between a μFE model and DEM for an assembly of spheres under triaxial compression, in: EPJ Web of Conferences, vol. 140, EDP Sciences, 2017, p. 15002.
- [33] T. Qiao, J. Li, S. Ji, A modified discrete element method for concave granular materials based on energy-conserving contact model, Theor. Appl. Mech. Lett. 12 (2) (2022) 100325.
- [34] A. Hrennikoff, Solution of problems of elasticity by the framework method, J. Appl. Mech. 8 (4) (1941) A169–A175.
- [35] M. Nikolić, E. Karavelić, A. Ibrahimbegovic, P. Miščević, Lattice element models and their peculiarities, Arch. Comput. Methods Eng. 25 (3) (2018) 753–784.
- [36] Z. Li, Z. Luo, L.-C. Zhang, C.-H. Wang, Topological design of pentamode lattice metamaterials using a ground structure method, Mater. Des. 202 (2021) 109523.
- [37] M. Ostoja-Starzewski, Lattice models in micromechanics, Appl. Mech. Rev. 55 (1) (2002) 35–60.
- [38] H. Yin, A simplified continuum particle model bridging interatomic potentials and elasticity of solids, J. Eng. Mech. 148 (5) (2022) 04022017.
- [39] H. Yin, Generalization of the singum model for the elasticity prediction of lattice metamaterials and composites, ASCE J. Eng. Mech. (2022), https://doi.org/ 10.1061/(ASCE)EM.1943-7889.0002152, in press.
- [40] H. Yin, J. Cui, L. Teka, M. Zadshir, Effect of wrapping force on the effective elastic behavior of packed cylinders, J. Appl. Mech. (2022) 1–32.

- [41] H. Yin, Improved singum model based on finite deformation of crystals with the thermodynamic equation of state, ASCE J. Eng. Mech. (2022), https://doi.org/10. 1061/JENMDT.EMENG-6831, in press.
- [42] E. Wigner, F. Seitz, On the constitution of metallic sodium, Phys. Rev. 43 (10) (1933) 804.
- [43] E.B. Tadmor, R.E. Miller, Modeling Materials: Continuum, Atomistic and Multiscale Techniques, Cambridge University Press, 2011.
- [44] B. Seth, Finite strain in elastic problems, Philos. Trans. R. Soc. Lond. Ser. A, Math. Phys. Sci. 234 (738) (1935) 231–264.
- [45] D. Gross, S. Kolling, R. Mueller, I. Schmidt, Configurational forces and their application in solid mechanics, Eur. J. Mech. A, Solids 22 (5) (2003) 669–692.
- [46] H. Hertz, Ueber die berührung fester elastischer k\u00f6rper (On the fixed elastic body contact), J. Reine Angew. Math. 92 (1882) 156-171.
- [47] R.D. Mindlin, H. Deresiewicz, Elastic Spheres in Contact Under Varying Oblique Forces, 1953.
- [48] K.L. Johnson, Contact Mechanics, Cambridge University Press, 1987.
- [49] H. Yin, L. Sun, G.H. Paulino, Micromechanics-based elastic model for functionally graded materials with particle interactions, Acta Mater. 52 (12) (2004) 3535–3543.
- [50] H. Yin, G. Paulino, W. Buttlar, L. Sun, Micromechanics-based thermoelastic model for functionally graded particulate materials with particle interactions, J. Mech. Phys. Solids 55 (1) (2007) 132–160.
- [51] A. Dewaele, P. Loubeyre, M. Mezouar, Equations of state of six metals above 94 GPa, Phys. Rev. B 70 (9) (2004) 094112.
- [52] M. Doyoyo, J.W. Hu, Multi-axial failure of metallic strut-lattice materials composed of short and slender struts, Int. J. Solids Struct. 43 (20) (2006) 6115–6139.
- [53] R. Al-Jishi, G. Dresselhaus, Lattice-dynamical model for alkali-metal—graphite intercalation compounds, Phys. Rev. B 26 (8) (1982) 4523.
- [54] X. Lu, X. Lin, M. Chiumenti, M. Cervera, Y. Hu, X. Ji, L. Ma, H. Yang, W. Huang, Residual stress and distortion of rectangular and S-shaped Ti-6Al-4V parts by directed energy deposition: modelling and experimental calibration, Addit. Manuf. 26 (2019) 166–179.